PHYSICAL REVIEW B **80**, 155135 (2009)

Universal features of coherent photonic thermal conductance in multilayer photonic band gap structures

Wah Tung Lau (留華東),[1,2,*] Jung-Tsung Shen (沈榮聰),[1,†] and Shanhui Fan (范汕洄)[1,2,‡]
[1]*Edward L. Ginzton Laboratory, Stanford University, Stanford, California 94305, USA*
[2]*Department of Electrical Engineering, Stanford University, Stanford, California 94305, USA*
(Received 26 May 2009; revised manuscript received 15 September 2009; published 28 October 2009)

We show that at the high-temperature limit, the coherent photonic thermal conductance of a multilayer photonic crystal can be significantly below the corresponding thermal conductance of vacuum. Moreover, the thermal conductance at this limit is independent of the thicknesses of the layers but dependent on the refractive indices of the layers only. Such universal features are directly related to the ergodic nature of the distribution of photonic bands in the frequency space.

DOI: 10.1103/PhysRevB.80.155135 PACS number(s): 44.40.+a, 42.70.Qs, 05.60.−k, 63.22.Np

I. INTRODUCTION

Photon is an important carrier of heat. Photonic crystals, with band gaps that affect the photon transport, therefore naturally have significant potentials for managing radiative heat transfer. Using photonic crystal structures to manipulate far-field thermal radiation into free space has been extensively studied in recent years.[1–19] Moreover, it has been noted that the transport properties of thermal photons *within* photonic crystals are strongly influenced by photonic band structures.[16]

An important technological goal for heat-transfer management is to reduce thermal conductance. Reducing the photonic thermal conductance, for example, can have significant implications in the developments of high-temperature thermal barrier coatings.[20] In this regard, from a fundamental perspective, a natural idea is to make use of photonic band gaps to suppress the thermal conductance, which is the subject of the present paper. Related to this idea, we note that the use of *phononic* band gap effect to reduce phononic thermal conductance has been considered for one-dimensional channels,[21] and for multilayer films.[22,23] Such conductance reduction requires thermal transport to be coherent.[24] Since interactions between photons are much weaker than phonons in most cases, coherent suppression of thermal conductance should be more readily achievable in thermal photonic systems.

In a previous publication,[25] we calculated numerically the three-dimensional thermal conductance of a multilayer photonic crystal. The three-dimensional thermal conductance of an exemplary system, which consists of alternate layers of dielectric and vacuum, is reproduced here in Fig. 1, where the dielectric layers were chosen to be intrinsic silicon, with electric permittivity $\varepsilon_{\mathrm{Si}}=11.7$, i.e., refractive index $n_{\mathrm{Si}} \equiv \sqrt{11.7}=3.42$.[26] Reference 25 demonstrated that such multilayer structures have a thermal conductance below that of vacuum in the high-temperature limit, due to the suppression of evanescent tunneling, and the presence of photonic band gaps.[25] Here, the high-temperature limit refers to the temperature range $T \gg T_0$, where $T_0 \equiv hc/(k_B a)$, with a being the lattice constant, h being the Planck constant, c being the speed of light, and k_B being the Boltzmann constant. Alternatively, at any given temperature T including the room temperature, such "high-temperature limit" corresponds to the use of a sufficiently large periodicity a. Similarly, the temperature $T \ll T_0$, or at a given temperature T with a small periodicity a, will be referred to as the "low-temperature limit."

In this paper, we show that in the high-temperature limit, the normalized thermal conductance with respect to vacuum in fact approaches a value that is *independent of the layer thicknesses*. This universal feature, which was not pointed out before, is remarkable because the suppression of thermal conductance arises from the photonic band gap effect and the properties of the photonic band structure strongly depend on the layer thicknesses. To explain this universal feature, we develop a complete analytical theory on the statistical distribution of the photonic bands in frequency space. Our theory indicates that the behavior of thermal conductance has a deep connection to the ergodic nature of the photonic band structure in these systems.

The paper is organized as follows. In Sec. II, we consider the high-temperature limit of the three-dimensional thermal

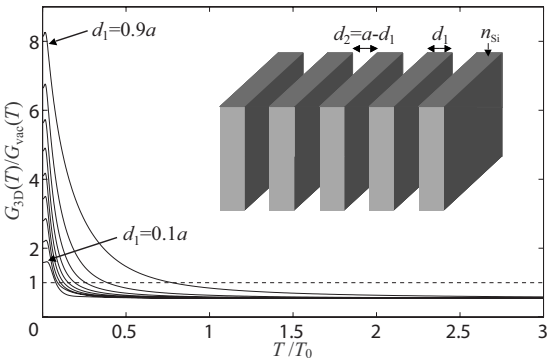

FIG. 1. Normalized three-dimensional thermal conductance $G_{3D}(T)/G_{vac}(T)$ versus normalized temperature T/T_0, for silicon-vacuum multilayer photonic crystals. Here $T_0 \equiv hc/(k_B a)$, where a is the lattice constant. The refractive index of silicon is $n_{\mathrm{Si}} \equiv \sqrt{11.7}=3.42$. The black solid curves correspond to structures with silicon thicknesses $d_1=0.1a, 0.2a, \ldots, 0.9a$, respectively. The corresponding vacuum thickness for each d_1 is $d_2=a-d_1$. For all structures, $\lim_{T\to\infty} G_{3D}(T)/G_{vac}(T)$ all converge to 0.548. The vacuum level $G_{3D}(T)/G_{vac}(T)=1$ is denoted by the dashed line.

conductance of a silicon-vacuum multilayer photonic crystal and demonstrate numerically that the conductance value at this limit is independent of the layer thicknesses. In Sec. III, we further show that such independence is present for each propagating direction and polarization, which we call *one-dimensional channel*. The analysis of a one-dimensional channel allows us to understand the behavior of the thermal conductance from the frequency distribution of photonic bands. In Sec. IV, we develop a theory for the frequency distribution of photonic bands. This theory indicates that the behavior of thermal conductance at the high-temperature limit is directly related to the ergodicity of the distribution and from which one could establish analytically the universal value for conductance at the high-temperature limit. In Secs. V and VI, we numerically verify the theory for one-dimensional channel and for three-dimensional thermal conductance, respectively. Finally, we summarize the paper in Sec. VII.

II. THREE-DIMENSIONAL THERMAL CONDUCTANCE IN MULTILAYER PHOTONIC CRYSTAL

Throughout this paper, we will be investigating the properties of photonic thermal conductance of a multilayer photonic crystal structure. For concreteness, we consider structures with periodically alternating layers of dielectrics and vacuum, with thicknesses d_1 and d_2, and dielectric constants $\varepsilon_1=n^2$ and $\varepsilon_2=1$, respectively. (Inset of Fig. 1 shows schematically the structure.)

For such a structure, at a given wave-vector component parallel to the layers $k_\parallel$ and polarization σ, its dispersion relation $\omega_m(K,k_\parallel,\sigma)$, which relates the frequency ω of a photon mode in the mth photonic band to the Bloch wave number K perpendicular to the layers, is obtained by[25,27,28]

$$\cos[K(d_1+d_2)]=\cos\left(\frac{\bar{n}_1 d_1}{c}\omega\right)\cos\left(\frac{\bar{n}_2 d_2}{c}\omega\right)-\xi\sin\left(\frac{\bar{n}_1 d_1}{c}\omega\right)\sin\left(\frac{\bar{n}_2 d_2}{c}\omega\right), \quad (1)$$

where

$$\bar{n}_{1,2}\equiv\sqrt{\varepsilon_{1,2}-\kappa^2}, \quad (2)$$

with $\kappa\equiv k_\parallel c/\omega$,

$$\xi\equiv\frac{1}{2}\left(\frac{P\bar{n}_1}{\bar{n}_2}+\frac{\bar{n}_2}{P\bar{n}_1}\right), \quad (3)$$

with $P=1$ for the $\sigma=s$ polarization (the electric field is parallel to the layers) and $P=\varepsilon_2/\varepsilon_1$ for the $\sigma=p$ polarization (the magnetic field is parallel to the layers).

At a given temperature T, the three-dimensional coherent thermal conductance is given by[25,31]

$$G_{3D}(T)=\frac{\partial}{\partial T}\sum_{\sigma=s,p}\int_0^\infty\frac{k_\parallel dk_\parallel}{2\pi}\sum_m\int_{K>0}\frac{dK}{2\pi}\times\frac{\partial\omega_m(K,k_\parallel,\sigma)}{\partial K}\frac{\hbar\omega_m(K,k_\parallel,\sigma)}{e^{\hbar\omega_m(K,k_\parallel,\sigma)/(k_BT)}-1}, \quad (4)$$

where $\hbar=h/(2\pi)$ is the reduced Planck constant.

Using Eq. (4), we plot in Fig. 1, the normalized thermal conductance $G_{3D}(T)/G_{vac}(T)$, for structures with different layer thicknesses. Here $G_{vac}(T)=\pi^2k_B^4T^3/(15\hbar^3c^2)$ is the three-dimensional thermal conductance of vacuum. For all structures, the lattice constant is fixed to be a while the thickness of the dielectric layers is varied from $0.1a$ to $0.9a$.

The behaviors of the normalized thermal conductance of all structures show similar characteristics. First, at low temperature, $G_{3D}(T)/G_{vac}(T)>1$, due to the evanescent tunneling of photons through the vacuum layers.[25] In particular, at the limit of $T\to0$, the normalized thermal conductance approaches a value that is determined by an average over the permittivity of the structure and is therefore dependent on the layer thicknesses. In the high-temperature regime, on the other hand, $G_{3D}(T)/G_{vac}(T)<1$. Thus the use of photonic crystals allows one to suppress thermal conductance to a level below that of vacuum. This suppression of conductance is due to the presence of photonic band gaps over the entire high-frequency regime in the photonic band structure.[25]

One of the most striking features that was not noted in all previous studies, however, is that in the high-temperature limit $T\gg T_0$, the normalized thermal conductance $G_{3D}(T)/G_{vac}(T)$ not only is smaller than 1 but also approaches the *same* value, which in the case of silicon-vacuum structures is numerically found to be 0.548, *independent of the layer thicknesses*. This universal feature is remarkable because the suppression of thermal conductance arises from the photonic band gap effect and the properties of the photonic band structure are strongly dependent on the layer thicknesses. In the following, we present a complete theory to explain such universal feature.

III. THERMAL CONDUCTANCE IN ONE-DIMENSIONAL CHANNELS

To understand the high-temperature limit of the three-dimensional thermal conductance, we notice that in Eq. (4), the term

$$G(T,k_\parallel,\sigma)=\frac{\partial}{\partial T}\sum_m\int_{K>0}\frac{dK}{2\pi}\frac{\partial\omega_m(K,k_\parallel,\sigma)}{\partial K}\frac{\hbar\omega_m(K,k_\parallel,\sigma)}{e^{\hbar\omega_m(K,k_\parallel,\sigma)/(k_BT)}-1} \quad (5)$$

represents the contribution of all modes for a given polarization and parallel wave vector. Below, we refer to each of such modes as a one-dimensional channel or *single channel*. The three-dimensional thermal conductance is closely related to the behaviors of such individual channel.

The conductance of such a one-dimensional channel can be simplified to obtain[29]

$$G(T,\kappa,\sigma)=k_B\int_0^\infty\frac{d\omega}{2\pi}\frac{[\hbar\omega/(k_BT)]^2e^{\hbar\omega/(k_BT)}}{[e^{\hbar\omega/(k_BT)}-1]^2}\Theta(\omega,\kappa,\sigma), \quad (6)$$

where $\Theta(\omega,\kappa,\sigma)=1$ when (ω,κ,σ) is in the photonic bands and $\Theta(\omega,\kappa,\sigma)=0$ in the photonic band gaps. In this and subsequent sections that treat a single channel, without loss of generality, we shall assume normal incidence $\kappa=0$ and a

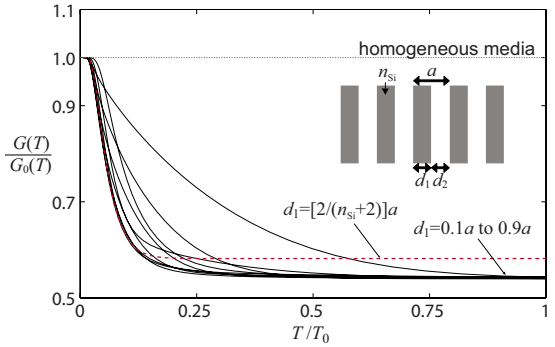

FIG. 2. (Color online) Normalized single-channel thermal conductance $G(T)/G_0(T)$ versus normalized temperature T/T_0 for silicon-vacuum multilayer photonic crystals with thermal photons of a single polarization at normal incidence ($\kappa=0$). Here $T_0 \equiv hc/(k_B a)$, where a is the lattice constant. The index of silicon is $n_{Si} \equiv \sqrt{11.7}=3.42$. d_1 denotes the silicon thickness and the vacuum thickness is $d_2=a-d_1$, as shown in the inset. The black solid lines represent the cases with $d_1=0.1a, 0.2a, \ldots, 0.9a$, respectively. For each case, the characteristic ratio $(n_{Si}d_1-d_2)/(n_{Si}d_1+d_2)$ is irrational and $\lim_{T\to\infty} G(T)/G_0(T)=0.540$. A special case $d_1=d_* \equiv [2/(n_{Si}+2)]a=0.369a$ is represented by the red dashed line. In this case, the characteristic ratio is a rational value of 1/3, which results in $\lim_{T\to\infty} G(T)/G_0(T)=0.582$. The case of the homogeneous single channel $G(T)/G_0(T)=1$ is denoted by the black dotted line.

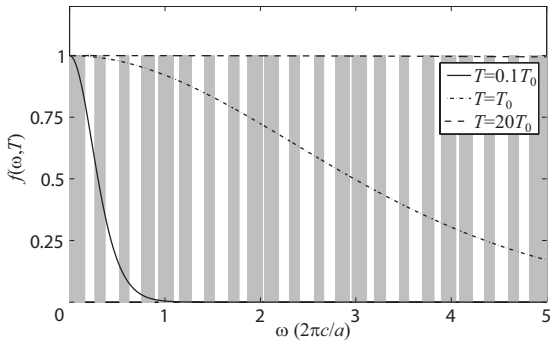

FIG. 3. Plot of $f(\omega,T)=[\hbar\omega/(k_B T)]^2 e^{\hbar\omega/(k_B T)}/[e^{\hbar\omega/(k_B T)}-1]^2$ versus ω for $T=0.1T_0$ (solid line), $T=T_0$ (dashed-dotted line), and $T=20T_0$ (dashed line). ω is in unit of $(2\pi c/a)$. $T_0 \equiv hc/(k_B a)$, where a is the lattice constant of the multilayer photonic crystal. The shaded regions denote the frequency ranges of the photonic bands of the crystal and the unshaded regions are the photonic band gaps. The case shown here is $d_1=d_2=0.5a$ and $n=n_{Si} \equiv \sqrt{11.7}$.

single polarization, and thus omit the labels κ and σ. Off-normal incidence with $\kappa \neq 0$ at a polarization σ corresponds to taking the layer indices and ξ according to Eqs. (2) and (3). For the special case of a uniform medium, one has $\Theta(\omega)=1$ for all frequencies and the contribution of a single one-dimensional channel from Eq. (6) is $G(T)=G_0(T)=\pi k_B^2 T/(6\hbar)$, which is the universal quantized thermal conductance for a single channel.[29–34]

In Fig. 2 we plot the normalized single-channel thermal conductance $G(T)/G_0(T)$ for different structures. The characteristics of $G(T)/G_0(T)$ are closely related to the dispersion relations of these multilayer structures. At low temperatures, $G(T)$ approaches $G_0(T)$, since only the modes in the first band in the vicinity of $\omega=0$ are thermally excited. As the temperature increases, the effect of band gaps becomes important and the normalized conductance $G(T)/G_0(T)$ is reduced below unity. In the high-temperature limit, as we shall see in more detail below, with few exceptions where a "characteristic ratio" $(nd_1-d_2)/(nd_1+d_2)$ is rational, all structures have the same normalized thermal conductance that is independent of layer thicknesses. Thus, the important features of the behaviors of three-dimensional thermal conductance are present in the single-channel thermal conductance as well.

To understand the high-temperature limit for thermal conductance in a single channel, we plot in Fig. 3 the temperature-dependent part of the integrand in Eq. (6), $f(\omega,T)=[\hbar\omega/(k_B T)]^2 e^{\hbar\omega/(k_B T)}/[e^{\hbar\omega/(k_B T)}-1]^2$, for several different temperatures T. Note that $0 \leq f(\omega,T) \leq 1$ for all T. In Fig. 3, we also plot the spectral positions of the photonic bands [shaded regions, $\Theta(\omega)=1$] and photonic band gaps [unshaded regions, $\Theta(\omega)=0$] for an exemplary structure. At each temperature, $2\pi G(T)/k_B$ is directly given by the total area of shaded regions bounded by $f(\omega,T)$ from Eq. (6). At high temperature, $f(\omega,T)$ is essentially 1 over a broad frequency range that encompasses many bands. The high-temperature limit of $G(T)/G_0(T)$ is thus

$$\lim_{T\to\infty} \frac{G(T)}{G_0(T)} = \eta = \lim_{\Lambda\to\infty} \frac{1}{\Lambda} \int_0^{\Lambda} d\omega \Theta(\omega), \tag{7}$$

where η describes the proportion of frequency ranges that are in the photonic bands over the entire frequency spectrum. The high-temperature limit of thermal conductance is thus directly related to the distribution of photonic bands in frequency space. As will be shown below, for fixed layer indices, η attains a universal value that is independent of the layer thicknesses.

IV. DISTRIBUTIONS OF PHOTONIC BANDS IN FREQUENCY SPACE

In this section, we develop a theory to compute η analytically. We first rewrite Eq. (1) as

$$\begin{aligned} \alpha(\omega) &\equiv \cos[K(d_1+d_2)] \\ &= \frac{1}{2}\left\{ \frac{(\xi+1)}{2} \cos\left[\frac{(n_1 d_1 + n_2 d_2)\omega}{c}\right] \right. \\ &\quad \left. - \frac{(\xi-1)}{2} \cos\left[\frac{(n_1 d_1 - n_2 d_2)\omega}{c}\right] \right\} \\ &= r_a \cos(\tau_a \omega) - r_b \cos(\tau_b \omega). \end{aligned} \tag{8}$$

Here $r_a \equiv (\xi+1)/2$ and $r_b \equiv (\xi-1)/2$ depend only on the layer indices while the two time scales $\tau_a \equiv (n_1 d_1 + n_2 d_2)/c$ and $\tau_b \equiv (n_1 d_1 - n_2 d_2)/c$ depend on both the indices and thicknesses of the layers. Note that $r_a - r_b = 1$ in all situations. When $-1 \leq \alpha(\omega) \leq 1$, the frequency ω is in the photonic bands, whereas the frequency regions with $|\alpha(\omega)|>1$ correspond to the photonic band gaps. $\Theta(\omega)$ can now be expressed in terms of $\alpha(\omega)$, with

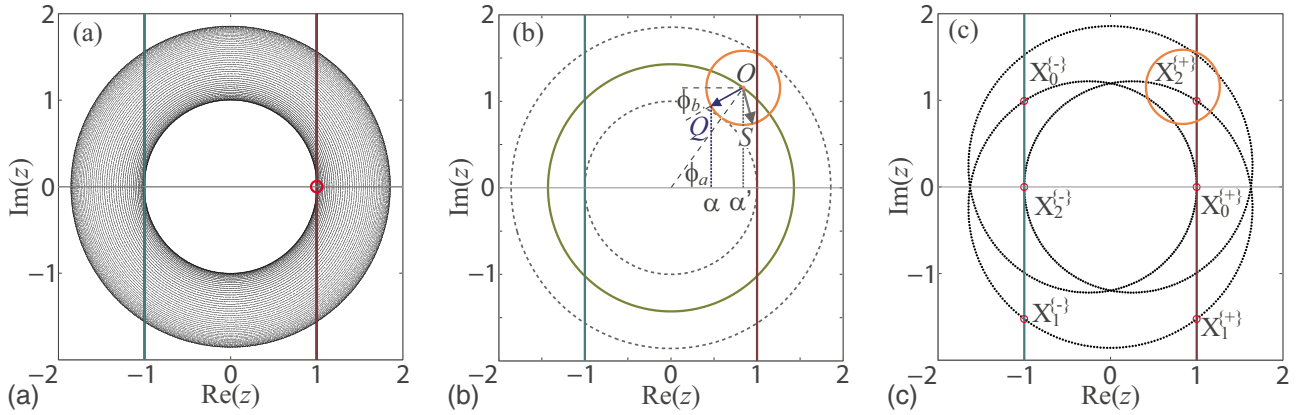

FIG. 4. (Color online) (a) Trajectory of $z(\omega)=r_a\exp(i\tau_a\omega)-r_b\exp(i\tau_b\omega)$ for incommensurate τ_a and τ_b. $z(\omega)$ is at $z=1$ when $\omega=0$ (small red ring) and is plotted as discrete points with frequency spacing $\Delta\omega=0.01(2\pi c/a)$. These points provide a dense coverage of the region $1\le|z|\le\xi$ and yield to a distribution pattern. The trajectory is generated using $n=n_{\mathrm{Si}}\equiv\sqrt{11.7}$ and $d_1=d_2=0.5a$. The distribution pattern is the same for other values of $d_{1,2}$ of the incommensurate case. $z(\omega)$ is restricted within the region bounded between $\mathrm{Re}(z)=-1$ (green solid line) and $\mathrm{Re}(z)=1$ (brown solid line) when ω is in the photonic bands. (b) Graphical representation of $z(\omega)$. The large circle (golden solid line) with radius r_a is centered at $z=0$. The small circle (orange solid line), with radius r_b, is centered at O where $z=r_a\exp(i\phi_a)$ and $r_a-r_b=1$. In all cases, $z(\omega)$ always starts at $z=1$ when $\omega=0$ and is bounded within $1\le|z|\le\xi$ for all ω. These boundaries are shown by gray dashed lines. When ω is in photonic bands, $z(\omega)$ is within the region between $\mathrm{Re}(z)=-1$ (green solid line) and $\mathrm{Re}(z)=1$ (brown solid line). The points Q, where $z(\omega=\phi_a/\tau_a)$, and S, where $z(\omega=\phi_a/\tau_a+2\pi/\tau_a)$, are on the same small circle. Here $\phi_a=0.3\pi$. (c) Trajectory of $z(\omega)$ for commensurate τ_a and τ_b. $z(\omega)$ is plotted as discrete points with frequency spacing $\Delta\omega=0.002(2\pi c/a)$ for $0\le\omega\le 2\pi N_a/\tau_a$. $z(\omega)$ intersects $\mathrm{Re}(z)=-1$ at the points $X_{i=0,1,2}^{\{-\}}$ and $\mathrm{Re}(z)=1$ at $X_{i=0,1,2}^{\{+\}}$, as marked by the small red rings. The case shown here is $n=n_{\mathrm{Si}}\equiv\sqrt{11.7}$ and $d_1=d_*=[2/(n_{\mathrm{Si}}+2)]a$ so that $\tau_b/\tau_a=N_b/N_a=1/3$. Other parameters are the same as in (a) and (b).

$$\Theta(\omega)=\begin{cases}0, & \text{if } |\alpha(\omega)|>1\\ 1, & \text{if } |\alpha(\omega)|\le 1\end{cases}. \tag{9}$$

To study the behavior of $\alpha(\omega)$, we consider a complex function,

$$z(\omega)\equiv r_a e^{i\tau_a\omega}-r_b e^{i\tau_b\omega}\equiv z_a(\omega)-z_b(\omega). \tag{10}$$

Notice that $\alpha(\omega)=\mathrm{Re}[z(\omega)]$. As ω increases while τ_a and τ_b are kept fixed, $z(\omega)$ traces out a trajectory in the complex z plane. An example of such trajectory with the characteristic ratio τ_b/τ_a chosen to be irrational, is shown in Fig. 4(a). In the figure, the continuous trajectory is discretized with $\Delta\omega=0.01(2\pi c/a)$ for visual aid. Thus, the calculation of η translates into determining the percentage of these points that lie in the region $|\mathrm{Re}[z(\omega)]|\le 1$. We note that these points are *not* uniformly distributed in the z plane.

To understand the distribution of the points $\{z(\omega):0\le\omega<\infty\}$, we first consider $z_a(\omega)$ and $z_b(\omega)$ separately. As ω varies, $z_a(\omega)$ distributes uniformly on a large circle (hereafter referred to as the "large circle") centered at $z=0$ with radius r_a [denoted by the golden line in Fig. 4(b)]. At each frequency ω, the actual location of $z(\omega)$ lies on a small circle (hereafter referred to as the "small circle"), centered at $z_a(\omega)$, with radius r_b where $r_b<r_a$.

Now consider two points $z(\omega')$ and $z(\omega'')$ with ω' and ω'' satisfying $\omega''-\omega'=2\pi/\tau_a$. Since $z_a(\omega')=z_a(\omega'')$, both points $z(\omega')$ and $z(\omega'')$ lie on the same small circle centered at $z_a(\omega')$, with their phase angles on the small circle separated by $2\pi\tau_b/\tau_a$ [Fig. 4(b)]. Hence, the set $\{z(\omega'+2\pi M/\tau_a)\}$, with M being integers, contains all the points of $z(\omega)$ that lie on this small circle. The distribution of such set of points on this small circle is critically dependent on whether τ_b/τ_a is rational. When τ_b/τ_a is irrational, i.e., τ_a and τ_b are incommensurate, the set $\{z(\omega'+2\pi M/\tau_a)\}$ uniformly covers the entire small circle, regardless of the actual value of τ_b/τ_a. This is known as the equidistribution theorem.[35] Alternatively, the argument above proves that $z(\omega)$ is ergodic in the complex z plane for the incommensurate case.[36] On the other hand, when τ_b/τ_a is rational, i.e., τ_a and τ_b are commensurate, such that $\tau_b/\tau_a=N_b/N_a$, with coprime integers N_a and N_b where $N_a>0$ and $-N_a\le N_b\le N_a$, there are only a finite number of points on this small circle, as the sequence $\{z(\omega'+2\pi M/\tau_a)\}$ is periodic with periodicity $M=N_a$.

First, we discuss the incommensurate case. From Fig. 4(b), we note that each point on the trajectory $z[\phi_a(\omega),\phi_b(\omega)]$ satisfies $\mathrm{Re}(z)=\alpha=r_a\cos\phi_a-r_b\cos\phi_b$, where ϕ_a is the phase angle on the large circle while ϕ_b is the phase angle on the small circle. Thus, for the incommensurate case, the distribution function for α is

$$\begin{aligned}\rho^{[I]}(\alpha)d\alpha&=\frac{1}{\pi}\int_0^\pi d\phi_a\frac{1}{\pi}[\phi_b(\phi_a,\alpha+d\alpha)-\phi_b(\phi_a,\alpha)]\\&=\frac{1}{\pi}\int_0^\pi d\phi_a\frac{1}{\pi}\left\{\mathrm{Re}\left[\cos^{-1}\left(\frac{r_a\cos\phi_a-\alpha-d\alpha}{r_b}\right)\right]\right.\\&\left.-\mathrm{Re}\left[\cos^{-1}\left(\frac{r_a\cos\phi_a-\alpha}{r_b}\right)\right]\right\}.\end{aligned} \tag{11}$$

For each ϕ_a, the integrand calculates the range of phase angles ϕ_b on the small circle that falls between $[\alpha,\alpha+d\alpha]$. Due to symmetry, only half the circles, with $0\le\phi_{a,b}\le\pi$, are needed to be considered in both cases. Hereafter, we will use the superscript $[I]$ to denote the "incommensurate case."

Writing $\alpha' = r_a \cos\phi_a$, Eq. (11) can be rewritten as

$$\rho^{[I]}(\alpha) = \int_{-r_a}^{r_a} d\alpha' \, \mathrm{Re}\left[\frac{1}{\pi\sqrt{r_a^2 - \alpha'^2}}\right] \mathrm{Re}\left[\frac{1}{\pi\sqrt{r_b^2 - (\alpha - \alpha')^2}}\right]. \tag{12}$$

On a side note, using the Bessel function identity: $J_0(r\varsigma) = \int_{-\infty}^{\infty} d\alpha \, \mathrm{Re}[1/(\pi\sqrt{r^2-\alpha^2})] e^{-i\varsigma\alpha}$, where J_0 is the zeroth-order Bessel function, $\rho^{[I]}(\alpha)$ can also be expressed in a compact form

$$\rho^{[I]}(\alpha) = \int_0^{\infty} \frac{d\varsigma}{\pi} J_0(r_a\varsigma) J_0(r_b\varsigma) \cos(\varsigma\alpha). \tag{13}$$

From Eq. (12), the proportion of frequencies in the photonic bands for the incommensurate case, $\eta^{[I]}$, is

$$\begin{aligned}\eta^{[I]} &= \int_{-1}^{1} d\alpha \int_{-r_a}^{r_a} d\alpha' \, \mathrm{Re}\left[\frac{1}{\pi\sqrt{r_a^2 - \alpha'^2}}\right] \\ &\quad \times \mathrm{Re}\left[\frac{1}{\pi\sqrt{r_b^2 - (\alpha - \alpha')^2}}\right] \\ &= \frac{1}{\pi^2} \int_0^{\pi} d\phi_a \left\{ \mathrm{Re}\left[\cos^{-1}\left(\frac{r_a \cos\phi_a - 1}{r_b}\right)\right] \right. \\ &\quad \left. - \mathrm{Re}\left[\cos^{-1}\left(\frac{r_a \cos\phi_a + 1}{r_b}\right)\right] \right\}. \end{aligned} \tag{14}$$

From Eq. (14), we see that $\eta^{[I]}$ is independent of the specific values of τ_a and τ_b, and hence is independent of the thicknesses of the layers in the incommensurate case.

For the commensurate cases, since $\tau_b/\tau_a = N_b/N_a$, $z(\omega)$ becomes periodic with periodicity $2\pi N_a/\tau_a$. As an example, in Fig. 4(c) we plot $z(\omega)$ for a commensurate case with $\tau_b/\tau_a = 1/3$. It is clearly seen that $z(\omega)$ is no longer ergodic in the complex z plane since it does not provide a dense coverage of an area in the complex z plane.

The value of η is directly given by the proportion of ω within $[0, \pi N_a/\tau_a]$ such that $-1 \le \mathrm{Re}[z(\omega)] \le 1$. Here only half the period of $z(\omega)$ needs to be considered since $z(\omega) = z^*(2\pi N_a/\tau_a - \omega)$. To find η, we first solve for all $\omega_j^{\{-\}}$ and $\omega_j^{\{+\}}$ that satisfy

$$\mathrm{Re}[z(\omega_j^{\{-\}})] = r_a \cos(\tau_a \omega_j^{\{-\}}) - r_b \cos(\tau_b \omega_j^{\{-\}}) = -1 \tag{15}$$

and

$$\mathrm{Re}[z(\omega_j^{\{+\}})] = r_a \cos(\tau_a \omega_j^{\{+\}}) - r_b \cos(\tau_b \omega_j^{\{+\}}) = 1, \tag{16}$$

for $0 \le j \le N_a - 1$. Then

$$\eta^{[C]}(N_a, N_b) = \frac{\tau_a}{\pi N_a} \sum_{j=0}^{N_a - 1} |\omega_j^{\{+\}} - \omega_j^{(-)}|. \tag{17}$$

Here the superscript $[C]$ denotes the "commensurate cases." Note that $\eta^{[C]}$ depends on N_a and N_b. Also for all values of N_a and N_b, $\omega_{j=0}^{\{+\}} = 0$ and $\eta^{[C]}(N_a, N_b) \ge \eta^{[I]}$.

In the Appendix, we give an alternate interpretation of the dynamics of $\mathrm{Re}[z(\omega)]$, where it is shown that $\eta^{[C]}(N_a, N_b)$ is proportional to the *length* of a finite trajectory and $\eta^{[I]}$ to an *area*. In general, as N_a increases, the trajectory becomes denser over the plane $1 \le |z| \le \xi$, and the difference between $\eta^{[C]}(N_a, N_b)$ and $\eta^{[I]}$ becomes smaller.

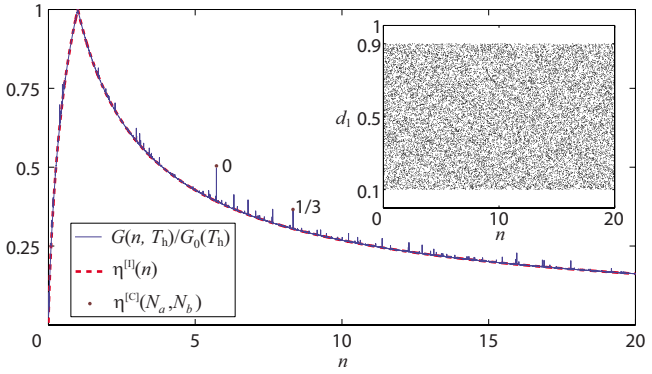

FIG. 5. (Color online) Normalized single-channel thermal conductance $G(n,T)/G_0(T)$ at the high-temperature limit versus the index n for dielectric-vacuum multilayer photonic crystals with various dielectric index and layer thicknesses. Here $T = T_h \equiv 20T_0$. The index of the dielectric layer n is varied continuously from $0 < n \le 20$. $\lim_{T\to\infty} G(T,n)/G_0(T)$ from the left-hand side of Eq. (7) is denoted by the blue solid line while $\eta(n)$ from the right-hand side of Eq. (7) is denoted by the red dashed line. For each value of n, the size of the dielectric layer is set by a random generator, with equal probability distribution in the range of $0.1a \le d_1 \le 0.9a$, as shown in the inset. The vacuum layer is set to be $d_2 = a - d_1$ accordingly. The two most prominent peaks, corresponding to the cases of $N_b/N_a = 0$ and $N_b/N_a = 1/3$, are marked as brown dots.

V. CONNECTIONS OF SINGLE-CHANNEL THERMAL CONDUCTANCE AND THE PROPORTION OF FREQUENCIES IN THE PHOTONIC BANDS

We now provide a detailed numerical test of Eq. (7), by comparing η as calculated theoretically in Sec. IV, with $\lim_{T\to\infty} G(T)/G_0(T)$ obtained numerically. We reiterate that for the incommensurate case, η calculated from Eq. (14) is independent of layer thicknesses. Since the structure is likely to belong to the incommensurate case with arbitrary choice of layer thicknesses, one should expect that for most structures, the high-temperature limit of the normalized thermal conductance is a function only of the refractive index and is independent of the thicknesses of the layers.

Here we provide a visual demonstration of such independence by computing $G(T)/G_0(T)$ in the high-temperature regime for various structures with different index values of the dielectric layer. For each index value, the width of the dielectric layer is randomly assigned a value within $0.1 \le d_1/a \le 0.9$ using a pseudorandom generator and the width of the vacuum layer is set as $d_2 = a - d_1$ accordingly. The operating temperature is fixed at $T_h \equiv 20T_0$, which according to Fig. 2, is well within the high-temperature regime of these structures.

The result of $G(n,T_h)/G_0(T_h)$ thus calculated, as a function of refractive index of the dielectric layer, is plotted in Fig. 5. In spite of the random choice of layer thicknesses, the result collapses onto a single universal curve that agrees precisely with $\eta^{[I]}(n)$, with a few discrete points of deviation that are due to the commensurate cases. Thus, the numerical

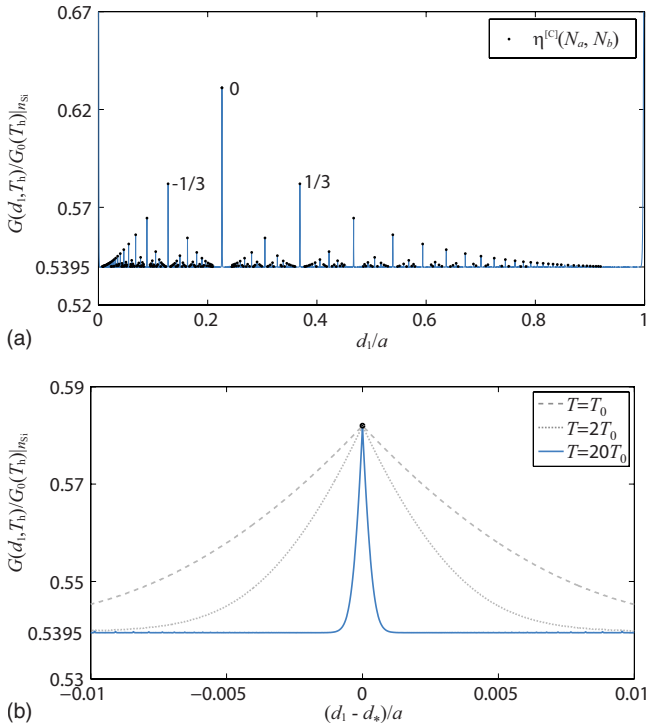

FIG. 6. (Color online) (a) Normalized single-channel thermal conductance $G(d_1,T)/G_0(T)$ at the high-temperature limit for various layer thicknesses (blue solid line), with silicon as the dielectric layers ($n_{Si} \equiv \sqrt{11.7} = 3.42$). Here $T = T_h \equiv 20T_0$. The size of dielectric layer is varied from $0 \le d_1 \le a$ and the vacuum layer is set at $d_2 = a - d_1$ accordingly. Though not shown, $G(d_1,T_h)/G_0(T_h)$ approaches 1 at $d_1 = 0$ or $d_1 = a$. The black dots are the theoretical values of $\eta^{[C]}(N_a,N_b)$ marked at $d_1 = a(N_a+N_b)/[n_{Si}(N_a-N_b)+(N_a+N_b)]$, for any coprime integers N_a and N_b satisfying $N_a > 0$ and $-N_a \le N_b \le N_a$. The values of $\eta^{[C]}(N_a,N_b)$ in the range $0 \le |N_b| \le N_a \le 20$ are calculated. N_b/N_a of the most pronounced peaks (0, 1/3, and −1/3) are labeled on the graph. (b) Same as (a), with $d_1 = d^* \equiv [2/(n_{Si}+2)]a$. Shown here are the cases of $T = 20T_0$ (blue solid line), $T = 2T_0$ (gray dotted line), and $T = T_0$ (gray dashed line). The black dot is the theoretical value of $\eta^{[C]}(N_a = 3, N_b = 1)$.

calculations validate the universality of the limit of thermal conductance suppression in these structures. Examining Fig. 5, we note that $G(n,T_h)/G_0(T_h)$ attains a maximum value of unity at $n = 1$, where there is no index contrast. It decreases on both sides of $n = 1$, as the index contrast increases. We have included cases with $n < 1$ for completeness purpose.

We now numerically validate the commensurate case. For this purpose, we fix the dielectric layer to be silicon with index n_{Si} and evaluate $G(d_1,T_h)/G_0(T_h)$ over a continuous range of $0 \le d_1 \le a$, with $d_2 = a - d_1$. For most choices of d_1, $G(d_1,T_h)/G_0(T_h)$ is at a constant value of 0.540, which is exactly the theoretical value of $\eta^{[I]}$ at this refractive index [Fig. 6(a)]. The deviation from this constant value occurs in a discrete set of peaks centered at $d_1 = a[(N_a+N_b)]/[n_{Si}(N_a-N_b)+(N_a+N_b)]$ that correspond to the commensurate cases with $\tau_b/\tau_a = N_b/N_a$. The peak values precisely match the theoretical values of $\eta^{[C]}(N_a,N_b)$ [Fig. 6(a)]. Thus, these numerical calculations provide a validation of the theory in Sec. II for all cases.

In Fig. 6(a), the most prominent peak is located at $d_1 = a/(n_{Si}+1) = 0.226a$, which corresponds to the case $N_b = 0$. For $N_b \neq 0$ and $|N_b| \neq N_a$, the peak value becomes smaller as N_a gets larger. In general, for large N_a, the deviation from the incommensurate case is small since in these cases, the trajectory of $z(\omega)$, while periodic, provides a fairly dense coverage of the complex plane. Finally, the cases where $N_b = N_a$ and $N_b = -N_a$ correspond to homogeneous media with $d_1 = 0$ and $d_1 = a$, respectively. In both cases, one has $G(d_1,T_h)/G_0(T_h) = 1$.

In the high-temperature limit, the linewidths of all the peaks in Fig. 6(a) vanish. The nonvanishing width of the peaks in Fig. 6(a) is due to the choice of a finite operating temperature $T_h < \infty$. Increasing the operating temperature simply decreases the linewidths of the peaks but not the peak values, as demonstrated in Fig. 6(b) at the neighborhood of an arbitrarily chosen peak.

VI. THERMAL CONDUCTANCE OF THREE-DIMENSIONAL MULTILAYER PHOTONIC CRYSTAL STRUCTURES

We now apply the knowledge of one-dimensional channels to understand the universal behaviors for the three-dimensional case. From Eq. (4), the three-dimensional thermal conductance can be rewritten as[25]

$$G_{3D}(T,n) = 2\pi k_B \sum_{\sigma=s,p} \int_0^\infty \kappa d\kappa \times \left[\int_0^\infty \frac{d\omega}{2\pi} f_{3D}(\omega,T)\Theta(\omega,\kappa,\sigma,n) \right], \quad (18)$$

where the temperature-dependent part in the integrand is

$$f_{3D}(\omega,T) \equiv \frac{\omega^2}{c^2} \frac{[\hbar\omega/(k_BT)]^2 e^{\hbar\omega/(k_BT)}}{[e^{\hbar\omega/(k_BT)} - 1]^2}. \quad (19)$$

Note that $f_{3D}(\omega,T) = (\omega/c)^2 f(\omega,T)$. At large T, it is smooth and slowly varying. Each single channel with distinct κ and polarization σ satisfies Eq. (7) individually. Also at the high-temperature limit, the contributions from photon channels within $\min(1,n) < \kappa \le \max(1,n)$ is negligible since it corresponds to evanescent tunneling process across the low-indexed layer. Consequently,

$$\lim_{T\to\infty} G_{3D}(T,n)/G_{vac}(T) = \eta_{3D}(n), \quad (20)$$

where

$$\eta_{3D}(n) \equiv \sum_{\sigma=s,p} \int_0^{\min(1,n)} \kappa d\kappa \left[\lim_{\Lambda\to\infty} \frac{1}{\Lambda} \int_0^\Lambda d\omega \Theta(\omega,\kappa,\sigma,n) \right] = \sum_{\sigma=s,p} \int_0^{\min(1,n)} \eta^{[I]}_{\sigma=s,p}(\kappa,n)\kappa d\kappa. \quad (21)$$

In Eq. (21), the cases with commensurate $\tau_a(\kappa) = \overline{n_1}d_1 + \overline{n_2}(a-d_1)$ and $\tau_b(\kappa) = \overline{n_1}d_1 - \overline{n_2}(a-d_1)$ occur at discrete values of κ and do not contribute to the integrals. Only the incommensurate cases contribute, and thus both

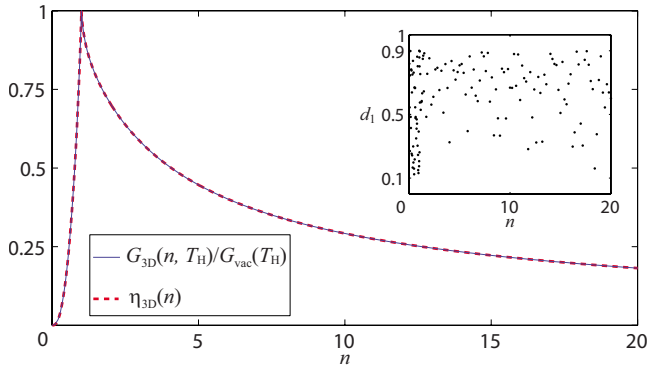

FIG. 7. (Color online) Normalized three-dimensional thermal conductance $G_{3D}(n,T)/G_{vac}(T)$ at the high-temperature limit versus n for various dielectric index and layer thicknesses. $T=T_H\equiv 25T_0$. The index of the dielectric layer n is varied continuously from $0<n\leq 20$. $\lim_{T\to\infty} G_{3D}(T,n)/G_{vac}(T)$ from the left-hand side of Eq. (20) is denoted by the blue solid line while $\eta_{3D}(n)$ from the right-hand side of Eq. (20) is denoted by the red dashed line. For each value of n, the size of the dielectric layer is set by a random generator, with equal probability in the range $0.1a\leq d_1\leq 0.9a$, as shown in the inset. The vacuum layer is set to be $d_2=a-d_1$ accordingly. At all data points, $G_{3D}(n,T_H)/G_{vac}(T_H)$ collapses onto the curve $\eta_{3D}(n)$ regardless of d_1.

η_{3D} and $\lim_{T\to\infty} G_{3D}(T)/G_{vac}(T)$ are independent of layer thicknesses.

To verify such independence, using Eqs. (18) and (19), we compute $G_{3D}(n,T_H)/G_{vac}(T_H)$ at $T_H=25T_0$, which is well within the high-temperature regime, for structures with various index values n of the dielectric layers. For each n, the dielectric layer thickness is randomly assigned a value within $0.1\leq d_1/a\leq 0.9$ and the vacuum layer thickness is then set by $d_2=a-d_1$. The plot of $G_{3D}(n,T_H)/G_{vac}(T_H)$ versus n is shown in Fig. 7. It collapses onto a single universal curve that matches $\eta_{3D}(n)$ precisely, regardless of the thicknesses of the layers. Note that unlike Fig. 5, there is no anomalous peak of commensurate cases, as expected from the discussions above.

VII. SUMMARY AND FINAL REMARKS

In summary, we have demonstrated the universal features of coherent photonic thermal conductance of multilayer photonic crystals. We have shown that the thermal conductance value at the high-temperature limit is independent of the layer thicknesses and depends on the refractive indices of the layers only. Such behavior is directly related to the ergodic nature of the distribution of photonic bands in frequency space.

For a given index contrast, our results set the lower bound for the normalized thermal conductance at high temperatures for structures consisting of two layers in each unit cell in most circumstances. In the intermediate-temperature regime, where T is comparable to T_0, other interesting behaviors of normalized thermal conductance may occur, which we will discuss in future publications. In the high-temperature regime, further reduction in normalized thermal conductance can only be achieved by either using a more complex unit cell or by breaking the periodicity. In all these cases, since the thermal conductance at the high-temperature limit is fundamentally a broadband effect, our initial results indicate that at such limit, similar universal features that are independent of many structural details can be obtained. These results will also be presented in future publications.

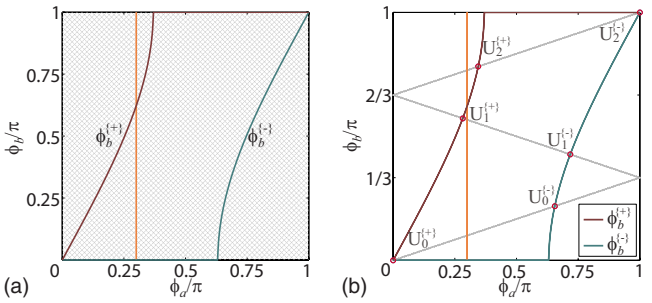

FIG. 8. (Color online) (a) Trajectory of $\alpha(\omega)=r_a\cos[\phi_a(\omega)]-r_b\cos[\phi_b(\omega)]$ for incommensurate τ_a and τ_b. $\alpha(\omega)$ is at $[\phi_a,\phi_b]=[0,0]$ when $\omega=0$ and is plotted as discrete points with frequency spacing $\Delta\omega=0.01(2\pi c/a)$. These points distribute uniformly on the plane. The case shown here is $n=n_{Si}\equiv\sqrt{11.7}$ and $d_1=d_2=0.5a$ [same as Fig. 4(a)]. The area bounded by $\phi_b^{\{-\}}(\phi_a)=\mathrm{Re}\{\cos^{-1}[(r_a\cos\phi_a+1)/r_b]\}$ (green solid curve) and $\phi_b^{\{+\}}(\phi_a)=\mathrm{Re}\{\cos^{-1}[(r_a\cos\phi_a-1)/r_b]\}$ (brown solid curve) is directly proportional to $\eta^{[I]}$. These two curves correspond to the lines at $\mathrm{Re}(z)=-1$ and $\mathrm{Re}(z)=1$ in Fig. 4, respectively. For comparison, the solid orange line at $\phi_a=0.3\pi$ is also drawn, which corresponds to the small circle (orange) in Figs. 4(b) and 4(c). (b) Same as (a), except that τ_a and τ_b are commensurate. The case shown here is when $n=n_{Si}\equiv\sqrt{11.7}$ and $d_1=[2/(n_{Si}+2)]a$ such that $\tau_b/\tau_a=N_b/N_a=1/3$ [same as Fig. 4(c)]. $\alpha(\omega)$ is plotted as discrete points with frequency spacing $\Delta\omega=0.002(2\pi c/a)$ for $0\leq\omega\leq\pi N_a/\tau_a$. $\alpha(\omega)$ intersects $\phi_b^{\{-\}}(\phi_a)$ at $U_{j=0,1,2}^{\{-\}}$ and $\phi_b^{\{+\}}(\phi_a)$ at $U_{j=0,1,2}^{\{+\}}$, as marked by the small red rings. The total length of line segments bounded by $\phi_b^{\{-\}}(\phi_a)$ and $\phi_b^{\{+\}}(\phi_a)$ is directly proportional to $\eta^{[C]}(N_a,N_b)$.

Regarding the practical applicability of the result, we have taken as an example, a temperature of $T=300$ K. This can be in the high-temperature limit for structures with $d_1/d_2\leq 9$, if we choose $a=10^{-4}$ m. At this temperature, nonnegligible contribution to thermal properties comes from photons with wavelength longer than 5 μm. Within such wavelength range, the real part of the dielectric constant only slightly varies from 11.66 to 11.74, and the field amplitude $1/e$ attenuation length is greater than 2×10^{-3} m over the entire wavelength range,[26] thus both material dispersion and material absorption can be safely ignored for the structure we considered here. There are certainly material systems, for example, systems supporting phonon-polariton excitations, for which significant dispersion and absorption can occur in the thermal wavelength range. The interplay of such phonon-polariton excitations with structural periodicity for thermal conduction is certainly of interest for future works.

As a final remark, in the high-temperature limit, thermal conductance involves contributions from a large number of states. Our results here indicate that certain general statistical characteristics of these states can strongly influence the thermal conductance behavior. While our analysis here applies

only to photons, we speculate that pursuing such a statistical analysis of state distribution might be fruitful for other thermal carriers as well.

ACKNOWLEDGMENT

This work is supported by AFOSR MURI Project No. FA9550-08-1-0407.

APPENDIX

Here we give an alternate graphical representation of $\alpha(\omega)=\mathrm{Re}[z(\omega)]$, which in particular facilitates the calculation for the commensurate case and also simplifies somewhat the calculation for the incommensurate case.

For the incommensurate case [Fig. 8(a)], by rewriting Eq. (14) we obtain

$$\eta^{[I]}=\frac{1}{\pi^2}\int_0^{\pi}d\phi_a\int_{\mathrm{Re}\{\cos^{-1}[(r_a\cos\phi_a-1)/r_b]\}}^{\mathrm{Re}\{\cos^{-1}[(r_a\cos\phi_a+1)/r_b]\}}d\phi_b. \quad \text{(A1)}$$

Thus $\eta^{[I]}$ is directly proportional to the *area* in the (ϕ_a,ϕ_b) plane that is bounded between the two curves,

$$\phi_b^{\{-\}}(\phi_a)=\mathrm{Re}\{\cos^{-1}[(r_a\cos\phi_a+1)/r_b]\} \quad \text{(A2)}$$

and

$$\phi_b^{\{+\}}(\phi_a)=\mathrm{Re}\{\cos^{-1}[(r_a\cos\phi_a-1)/r_b]\}. \quad \text{(A3)}$$

For each of the commensurate cases with $\tau_b/\tau_a=N_b/N_a$ [Fig. 8(b)], one needs to consider the trajectory of $[\phi_a(\omega),\phi_b(\omega)]$ as the frequency is varied. Such trajectory is a straight line $[\tau_a\omega,\tau_b\omega]$ that is folded into the irreducible region $[0\le\phi_a(\omega)\le\pi,0\le\phi_b(\omega)\le\pi]$. As the frequency increases from $\omega=0$, the trajectory starts at $(\phi_a,\phi_b)=(0,0)$. It then follows a straight line with the direction set by $\tau_b/\tau_a=N_b/N_a$. The trajectory "reflects" when it reaches the edges of the irreducible region. Moreover, it rebounds and traces back the incident path when it reaches one of the corners: $(\phi_a,\phi_b)=(0,\pi)$, $(\pi,0)$, or (π,π) at $\omega=\pi N_a/\tau_a$. Thus, for each of the commensurate cases, the trajectory does not provide a dense coverage of the irreducible region. Since the points are uniformly distributed along the trajectory, η is proportional to the total *length* of line segments bounded within the curves $\phi_b^{\{-\}}(\phi_a)$ and $\phi_b^{\{+\}}(\phi_a)$. Note that the total number of such line segments is N_a. On the other hand, when τ_a and τ_b are incommensurate, the trajectory never reaches the corners and so *uniformly* covers the entire region as $\omega\to\infty$, regardless of the exact values of τ_a and τ_b.

*wahtung@gmail.com
†jushen@gmail.edu
‡shanhui@stanford.edu

[1] C. M. Cornelius and J. P. Dowling, Phys. Rev. A **59**, 4736 (1999).
[2] S.-Y. Lin, J. G. Fleming, E. Chow, J. Bur, K. K. Choi, and A. Goldberg, Phys. Rev. B **62**, R2243 (2000).
[3] J.-J. Greffet, R. Carminati, K. Joulain, J.-P. Mulet, S. Mainguy, and Y. Chen, Nature (London) **416**, 61 (2002).
[4] S. Y. Lin, J. Moreno, and J. G. Fleming, Appl. Phys. Lett. **83**, 380 (2003).
[5] S.-Y. Lin, J. G. Fleming, and I. E.-Kady, Appl. Phys. Lett. **83**, 593 (2003).
[6] S.-Y. Lin, J. G. Fleming, and I. E.-Kady, Opt. Lett. **28**, 1909 (2003).
[7] C. Luo, A. Narayanaswamy, G. Chen, and J. D. Joannopoulos, Phys. Rev. Lett. **93**, 213905 (2004).
[8] I. Celanovic, D. Perreault, and J. Kassakian, Phys. Rev. B **72**, 075127 (2005).
[9] M. Florescu, H. Lee, A. J. Stimpson, and J. Dowling, Phys. Rev. A **72**, 033821 (2005).
[10] W. W. Chow, Phys. Rev. A **73**, 013821 (2006).
[11] M. Laroche, R. Carminati, and J.-J. Greffet, Phys. Rev. Lett. **96**, 123903 (2006).
[12] D. L. C. Chan, M. Soljacic, and J. D. Joannopoulos, Phys. Rev. E **74**, 016609 (2006).
[13] D. L. C. Chan, M. Soljacic, and J. D. Joannopoulos, Phys. Rev. E **74**, 036615 (2006).
[14] D. L. C. Chan, M. Soljačić, and J. D. Joannopoulos, Opt. Express **14**, 8785 (2006).
[15] J. C. W. Lee and C. T. Chan, Appl. Phys. Lett. **90**, 051912 (2007).
[16] M. Florescu, K. Busch, and J. P. Dowling, Phys. Rev. B **75**, 201101(R) (2007).
[17] S. E. Han, A. Stein, and D. J. Norris, Phys. Rev. Lett. **99**, 053906 (2007).
[18] S. John and R. Wang, Phys. Rev. A **78**, 043809 (2008).
[19] M. Diem, T. Koschny, and C. M. Soukoulis, Phys. Rev. B **79**, 033101 (2009).
[20] V. Shklover, L. Braginsky, G. Witz, M. Mishrikey, and C. Hafner, J. Comput. Theor. Nanosci. **5**, 862 (2008).
[21] A. N. Cleland, D. R. Schmidt, and C. S. Yung, Phys. Rev. B **64**, 172301 (2001).
[22] G. Chen, ASME J. Heat Transfer **121**, 945 (1999).
[23] M. V. Simkin and G. D. Mahan, Phys. Rev. Lett. **84**, 927 (2000).
[24] W. Kim, R. Wang, and A. Majumdar, Nanotoday **2**, 40 (2007).
[25] W. T. Lau, J.-T. Shen, G. Veronis, S. Fan, and P. V. Braun, Appl. Phys. Lett. **92**, 103106 (2008).
[26] E. D. Palik, *Handbook of Optical Constants of Solids* (Academic, New York, 1985), p. 554.
[27] A. Yariv and P. Yeh, *Photonics: Optical Electronics in Modern Communications*, 6th ed. (Oxford University Press, Oxford, England, 2007).
[28] R. de L. Kronig and W. A. Penney, Proc. R. Soc. London, Ser. A **130**, 499 (1931).
[29] L. G. C. Rego and G. Kirczenow, Phys. Rev. Lett. **81**, 232 (1998).
[30] L. G. C. Rego and G. Kirczenow, Phys. Rev. B **59**, 13080 (1999).
[31] K. Schwab, E. A. Henriksen, J. M. Worlock, and M. L. Roukes, Nature (London) **404**, 974 (2000).
[32] T. Yamamoto, S. Watanabe, and K. Watanabe, Phys. Rev. Lett.

92, 075502 (2004).
[33] D. R. Schmidt, R. J. Schoelkopf, and A. N. Cleland, Phys. Rev. Lett. **93**, 045901 (2004).
[34] M. Meschke, W. Guichard, and J. P. Pekola, Nature (London) **444**, 187 (2006).
[35] R. Beals, *Analysis: An Introduction* (Cambridge University Press, Cambridge, 2004).
[36] J.-P. Eckmann and D. Ruelle, Rev. Mod. Phys. **57**, 617 (1985).